buildings

MDPI

Article

Interaction Mechanism of Cementitious Composites Containing Different Twisted PVA Fiber Bundles

Hongmei Zhang, Fan Hu, Yuanfeng Duan *, Jiaqi Yang, Zhengteng Duan and Lening Cao

College of Civil Engineering and Architecture, Zhejiang University, Hangzhou 310058, China; zhanghongmei@zju.edu.cn (H.Z.); fanwindyhu@zju.edu.cn (F.H.); 22112069@zju.edu.cn (J.Y.); duanzt@zju.edu.cn (Z.D.); caolenimg@126.com (L.C.)

* Correspondence: ceyfduan@zju.edu.cn

Abstract: Fiber-reinforced cementitious composites (FRCCs) have made significant progress in improving the tensile and flexural properties of concrete members. Studies have shown that polyvinyl alcohol (PVA) fibers can effectively enhance the toughness of FRCCs, but the haphazard distribution of short-cut fibers makes it difficult to give full play to the high tensile strength of the fibers, and it is difficult for bundled fibers to effectively bond with the concrete substrate, which has become a challenge in the study of changing materials. Twisting the fibers by a physical process to improve the bonding performance of PVA fibers with FRCC substrate is a safe and feasible solution. However, research on silicate cementitious composites reinforced with twisted PVA fibers is limited. In this study, the interaction mechanism of through-length twisted PVA FRCCs with different twist factors and fiber bundle numbers was investigated. A concrete matrix material configured from silicate cement, fly ash, silica fume, and medium sand, in which PVA fibers with different twist factors were pre-incorporated, was used for the tests. Three-point bending tests were carried out on specimens with different twist factors (0, 50, 100, and 150 twists per meter) and fiber bundle numbers 1, 2, and 3. Compared to the untwisted PVA fiber specimens, the twist factor of 100 and the single fiber bundle specimens showed significant improvements in the bending properties, including a 36% increase in deflection, a 68% increase in the equivalent bending stress, and a 119% increase in energy consumption. Micro-X-ray computed tomography scans showed improved bending properties and energy consumption capabilities due to enhanced bonding properties as a result of the increased fiber–matrix interaction area and surface toughness.

Keywords: PVA fiber; twist; three-point flexural properties; toughness; microscopic mechanism; silicate cement

check for updates

Citation: Zhang, H.; Hu, F.; Duan, Y.; Yang, J.; Duan, Z.; Cao, L. Interaction Mechanism of Cementitious Composites Containing Different Twisted PVA Fiber Bundles. *Buildings* **2023**, *13*, 2194. https://doi.org/10.3390/buildings13092194

Academic Editor: Harry Far

Received: 28 July 2023
Revised: 18 August 2023
Accepted: 23 August 2023
Published: 29 August 2023

Copyright: © 2023 by the authors. Licensee MDPI, Basel, Switzerland. This article is an open access article distributed under the terms and conditions of the Creative Commons Attribution (CC BY) license (https://creativecommons.org/licenses/by/4.0/).

1. Introduction

Silicate cementitious composites are currently the most extensively employed materials in concrete structures, owing to their widespread availability, straightforward preparation, and superior mechanical properties [1,2]. However, these composites are frequently blended with other materials instead of being utilized independently due to their constrained mechanical properties for practical applications [3–5]. Fibers such as glass fiber, basalt fiber, forta-ferro fiber, coconut fiber, sisal fiber, steel fiber, and polyvinyl alcohol (PVA) fiber have been effectively used to reinforce silicate cement-based concrete [6–13]. Ozkilic et al. discovered that incorporating dispersed reinforcement of lightweight expanded clay concrete with coconut fiber and sisal fiber yielded a favorable impact on its mechanical properties, including the compressive strength and bending strength [7]. Prakash et al. noted that the inclusion of steel fibers in eco-concrete led to a decrease in slump, as well as improvements in the compressive strength, modulus of elasticity, split tensile strength, and flexural strength [12]. In general, an extensive body of research indicates that fiber-reinforced cementitious composites (FRCCs) showcase enhanced mechanical properties, pseudo-strain hardening behavior, elevated damage tolerance, and heightened cracking

resistance [14–18]. Armed with these superior material properties, there is a growing adoption of FRCCs for application in ductile components [19,20].

Due to their high aspect ratio, high ultimate tensile strength, relatively high modulus of elasticity, good chemical compatibility with silicate cement, and lack of health risks, PVA fibers have been widely used in reinforcing cementitious composites [21–23]. To achieve homogeneous toughening of the specimen, long PVA fibers are typically cut into short bundles of 6–24 mm and uniformly dispersed throughout the matrix [24]. Noushini et al. examined the dynamic and material properties of an FRCC with varying lengths of short-cut PVA fibers, finding improved mechanical properties but minimal impact on the damping characteristics [21]. The irregular arrangement of short-cut fibers limits harnessing their high tensile strength, while bundled fibers struggle to form effective bonds with the concrete surface, posing a challenge to exploring material modifications [25]. As a result, increasing attention has been paid to developing chemical additives to enhance the bonding performance between PVA fibers and the matrix [26,27]. Cao et al. used calcium carbonate whiskers as chemical additives with PVA and steel fibers to form a new cementitious composite for a bending test [26]. The $CaCO_3$ whiskers were shown to enhance the bonding performance between the fibers and the matrix, providing a crack resistance effect at the microscale. Due to the potential for complex chemical reactions to occur between additives and the cement matrix, resulting in the uncontrollable performance of specimens reinforced with fibers with relevant additives, improving the bonding of PVA fibers to the cement-based matrix from the fibers themselves is a sensible approach.

Many styles of short steel fibers have been developed to toughen cementitious materials due to their good processability, including fibers with roughened surfaces, round fibers with end paddles/buttons, hooked fibers, and twisted fibers [16,28–30]. Karalar et al. discovered a substantial enhancement in bending performance through the incorporation of waste lather scarps, akin to twisted steel fibers, into concrete, as demonstrated in a two-point bending test [30]. However, PVA fibers are only available in powder form or processed into filament or band form due to their poor processability [21]. Therefore, it may be possible to use twisted PVA fibers to address the limitations of flat fibers. Twisted fiber-based materials have been widely studied in fields such as textiles, robotics, and medicine for their high efficiency, fast response, scalability, long life, and improved tensile and bending capacity [31–33]. Haines et al. demonstrated an artificial muscle made of twisted PA6 fiber that can lift over 100 times the weight of human muscle at the same length and weight, owing to its improved tensile and flexural properties [32].

However, there are few studies in the literature on twisted PVA fiber-reinforced silicate cement-based composites. To implement the fiber-twisting process conveniently and to explore this concept, the reinforcement of through-length twisted fiber bundles is proposed, instead of uniformly distributed short fibers. The flexural properties of construction materials, which include the ability to absorb energy and maintain structural performance during bending behaviors, are of great importance to the ductile properties of structural members [20,34,35]. Drawing on these considerations and previous research [36,37], this paper examines the impact of various twist factors (0, 50, 100, 150 twists per meter) and fiber bundle quantities (1, 2, 3) on the flexural performance of through-length twisted PVA fiber-reinforced cementitious composites (TLTP-FRCCs). To account for the draping effect of PVA fibers and the size requirements of the flexural specimen, a specimen size of 160 × 40 × 15 mm was adopted [38]. To reduce the test variability, three specimens were fabricated for each test case. Therefore, three-point bending tests were conducted on 36 rectangular specimens to investigate the influence of fiber twisting on the flexural behavior of an FRCC [38]. Through macroscopic mechanical tests, microscopic observations, and relevant analysis, this study investigates the impact of four twist factors and three bundle numbers on the interaction mechanism of cementitious composites containing different twisted PVA fiber bundles. Additionally, the toughening mechanisms of twisting are revealed. This study recommends the optimal match of these two factors for ductile precast concrete components, among other applications.

2. Testing Design

This study investigates four twist factors (0, 50, 100, 150) and three bundle numbers (1, 2, 3) to comprehensively analyze the effect of twist factors and fiber bundle numbers on the interaction mechanism of TLTP-FRCC. To examine the PVA fiber bundle used, environmental scanning electron microscopy (ESEM) [34] was utilized to observe the bundle at a microscopic level. A removable mold made of nylon was designed and produced to meet the requirement for twisting and the size of the flexural specimen. After fabricating the specimens using the aforementioned mold, micro-X-ray computed tomography (MXCT) [39] was employed to observe the twisted PVA fiber bundle inside the unbent specimen at a micro level, which serves as a reference for comparing with the bent specimens.

2.1. Materials of TLTP-FRCC

The main matrix components used in this study, encompassing silicate cement, fly ash, silica fume, and medium sand, were pre-mixed, as illustrated in Figure 1a. The silicate cement had weight percentages of approximately 2.59%, 1.46%, and 0.019% for SO_3, MgO, and Cl^-, respectively, and demonstrated 3-day bending and compressive strengths of around 6.5 MPa and 37 MPa, respectively. The fly ash had a density of about 1.3 g/cm^3 and a total weight percentage of approximately 77% for SiO_2, Al_2O_3, and Fe_2O_3. The silica fume had a weight percentage of roughly 94% for SiO_2. The medium sand aggregate used had a particle size of 40–70 mesh and a weight percentage of approximately 93.0% for SiO_2. The long PVA fiber bundles used in this research were manufactured by Sinopec Chongqing SVW Chemical Co., Ltd., Chongqing, China, as depicted in Figure 1b. Table 1 presents the mechanical properties of the PVA fiber bundle with a slenderness of 2000 dtex/1000f.



(**a**) (**b**)

Figure 1. Physical images of materials used: (**a**) dry matrix powder; (**b**) PVA fiber.

Table 1. Material properties of the PVA fiber.

Diameter (μm)	Tensile Strength (MPa)	Elongation (%)	Elastic Modulus (Gpa)
17	1600	6–8	40

After conducting the trial mixing, a water–cement ratio of 0.34 was selected. The mix design of the cementitious composites is outlined in Table 2. This dry powder mix is a fiber-toughened cementitious mix with a strength of about 60 Mpa, configured in previous studies by the research group.

Table 2. Mix design of cementitious composites (kg/m^3).

Silicate Cement	Fly Ash	Silica Fume	Medium Sand	Water
702.6	122.2	61.1	1197.5	301.2

2.2. Microstructure of the PVA Fiber Bundle

To examine the microscopic morphology of the PVA fiber bundle, a bundle of PVA fiber was immobilized using epoxy resin and outer tape and observed with ESEM. The resulting images at two magnification levels are shown in Figure 2. In Figure 2a, it can be observed that the diameter of a bundle of the PVA fiber with epoxy resin was approximately 1600 μm. Figure 2b shows that the cross-section of a single PVA filament was a flat oval shape, and the gaps between the filaments were easily produced. However, a large number of fiber filaments can be coalesced into a whole under the action of epoxy resin.

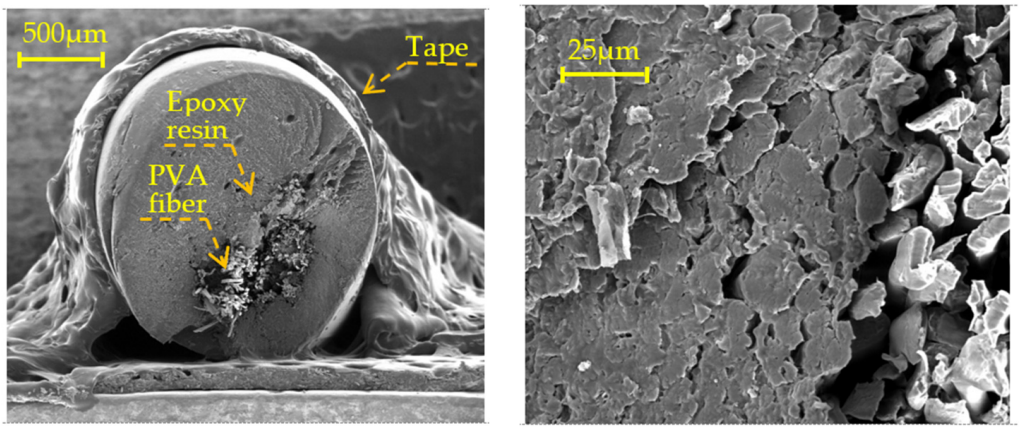


Figure 2. ESEM images of PVA fiber at two magnification levels: (**a**) 500 μm; (**b**) 25 μm.

2.3. Specimen Design and Preparation

To investigate the impact of through-length twisted PVA fiber on the bending capacity of concrete, various types of specimens were prepared for comparison, as outlined in Table 3. For the purpose of minimizing the test variability, three specimens were produced for each test case. The specimen number indicates the type, for instance, for B-2-1-3, 2 denotes two through-length fiber bundles, 1 denotes the first twisting condition, and 3 denotes the third parallel specimen for that case. The specially designed mold for the test is displayed in Figure 3; it could create 12 specimens at once, each measuring 160 × 40 × 15 (mm^3), and accommodate the arrangement of 0–3 through-length fibers. Additionally, the mold was constructed from nylon and assembled to facilitate mold removal, while also preventing any potential impact of the lubricants on the performance of the specimen. The empty slot in the center of the mold aided in securing and twisting the fibers. The specimen preparation procedure is depicted in Figure 4. First, the PVA fibers were arranged in the mold according to the working conditions indicated in Table 3. Second, the dry materials (silicate cement, fly ash, silica fume, and medium sand) were mixed with water in a mixer for five minutes to ensure thorough dispersion. Third, the well-mixed composites were poured into each mold along the edge to avoid altering the position and tension of the fibers. After vibration and smoothing, the surface was covered with cling film to prevent surface cracking caused by moisture evaporation. The specimens were left to cure for two days, after which they had attained the required strength for demolding and could be removed from the mold and placed in the maintenance room for steam curing for 26 days.

Table 3. Details of specimens.

Specimens	Bundles	Twist Factor
B-1-1-(1–3)	1	0
B-2-1-(1–3)	2	
B-3-1-(1–3)	3	
B-1-2-(1–3)	1	50
B-2-2-(1–3)	2	
B-3-2-(1–3)	3	
B-1-3-(1–3)	1	100
B-2-3-(1–3)	2	
B-3-3-(1–3)	3	
B-1-4-(1–3)	1	150
B-2-4-(1–3)	2	
B-3-4-(1–3)	3	

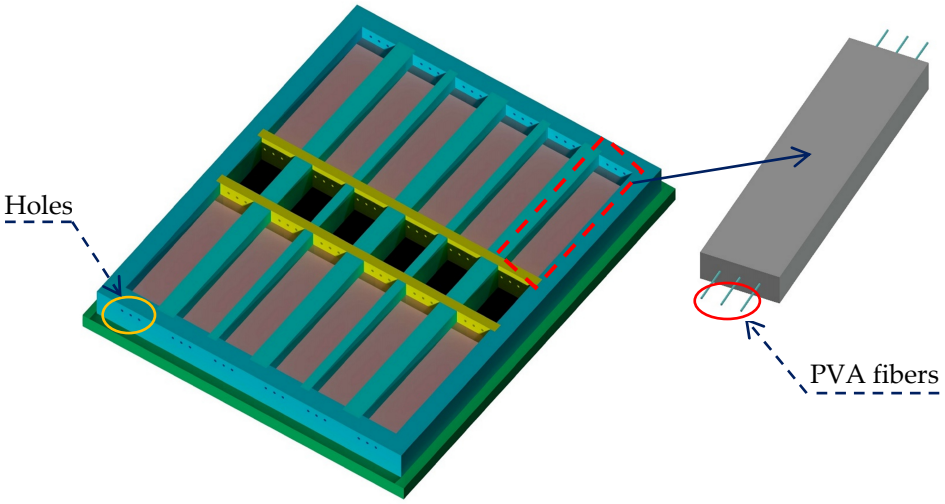


Figure 3. Conceptual drawing of the designed mold.

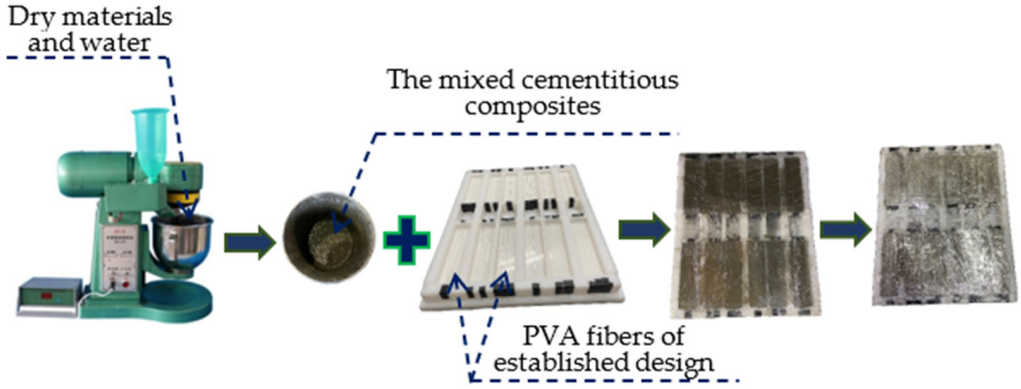


Figure 4. Specimen preparation process.

The macroscopic morphology of the fiber bundles at different twist factors is shown in Figure 5a, where it can be observed that the fiber bundles gradually transformed from flat sheets into spiral shapes with decreasing diameters as the twist factor increased. To examine the morphology of the PVA fiber bundles after the specimens were formed, MXCT was performed using the Nikon XTH320 MXCT facility at Zhejiang University, Hangzhou, China, as shown in Figure 5b. The scanning parameters used included an exposure time of 500 ms, a voltage of 200 kV, a current of 100 μA, and a scanning accuracy of approximately 30 μm [40]. Image processing was performed using VGStudio MAX 3.0 software, and

2D slices and 3D solid images were obtained by reconstructing the data from the original MXCT data. To capture the twisted fiber bundle morphology more accurately, specimen B-3-4-2 was selected, which contained three bundles of fibers and a twist factor of 150, for MXCT imaging in this study. The corresponding 3D reconstruction results are shown in Figure 5c, where it can be seen that the twisted fiber bundles were uniformly tensed in the specimen, and the twisted pattern, even the bubbles, is clearly visible.

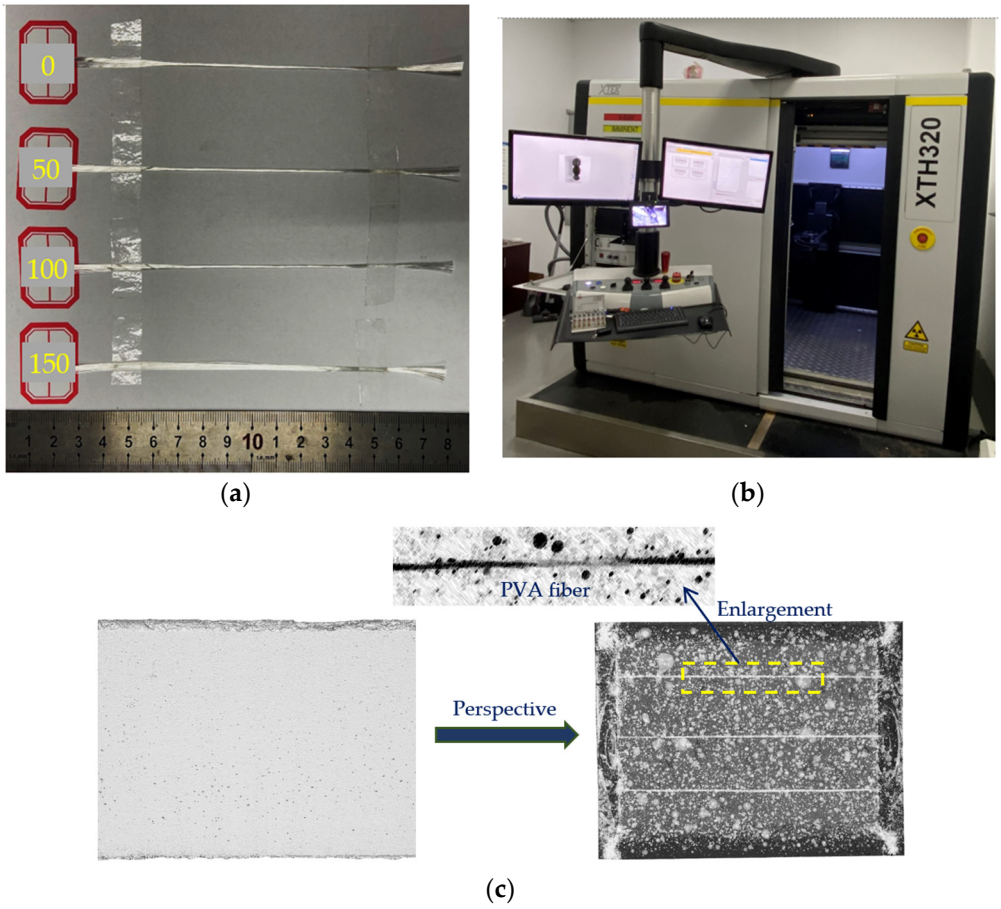


Figure 5. Morphology of twisted PVA fiber bundles: (**a**) macroscopic morphology before specimen formation (the value on the label is the relevant twist factor); (**b**) Nikon XTH320 MXCT facility at Zhejiang University; (**c**) 3D reconstruction of the specimen interior.

3. Flexural Behavior Testing

The INSTRON-8802 Electron-hydraulic Servo Fatigue Testing Machine (with a maximum applied load of 250 kN) was used to conduct the three-point flexural test on the rectangular specimens under displacement control, with a loading speed of 0.2 mm/min [41], as depicted in Figure 6a. To improve the clarity, both the enlarged view of the test setup enclosed in the red box of Figure 6a and its wireframe diagram are presented in Figure 6c, revealing that the test specimen dimensions were 160 × 40 × 15 mm, and the clear span was 120 mm. Carbon fiber fabrics and aluminum plates to reinforce the ends of the specimens in this study were used to avoid damage to the ends of the specimens, which would affect the test results, as illustrated in Figure 6b. The MLONT-F10 Linear Variable Displacement Transducer (LVDT) was utilized to measure the span deflection value of the specimen during the test, with a maximum range of 10 mm and a measurement accuracy of 1‰.

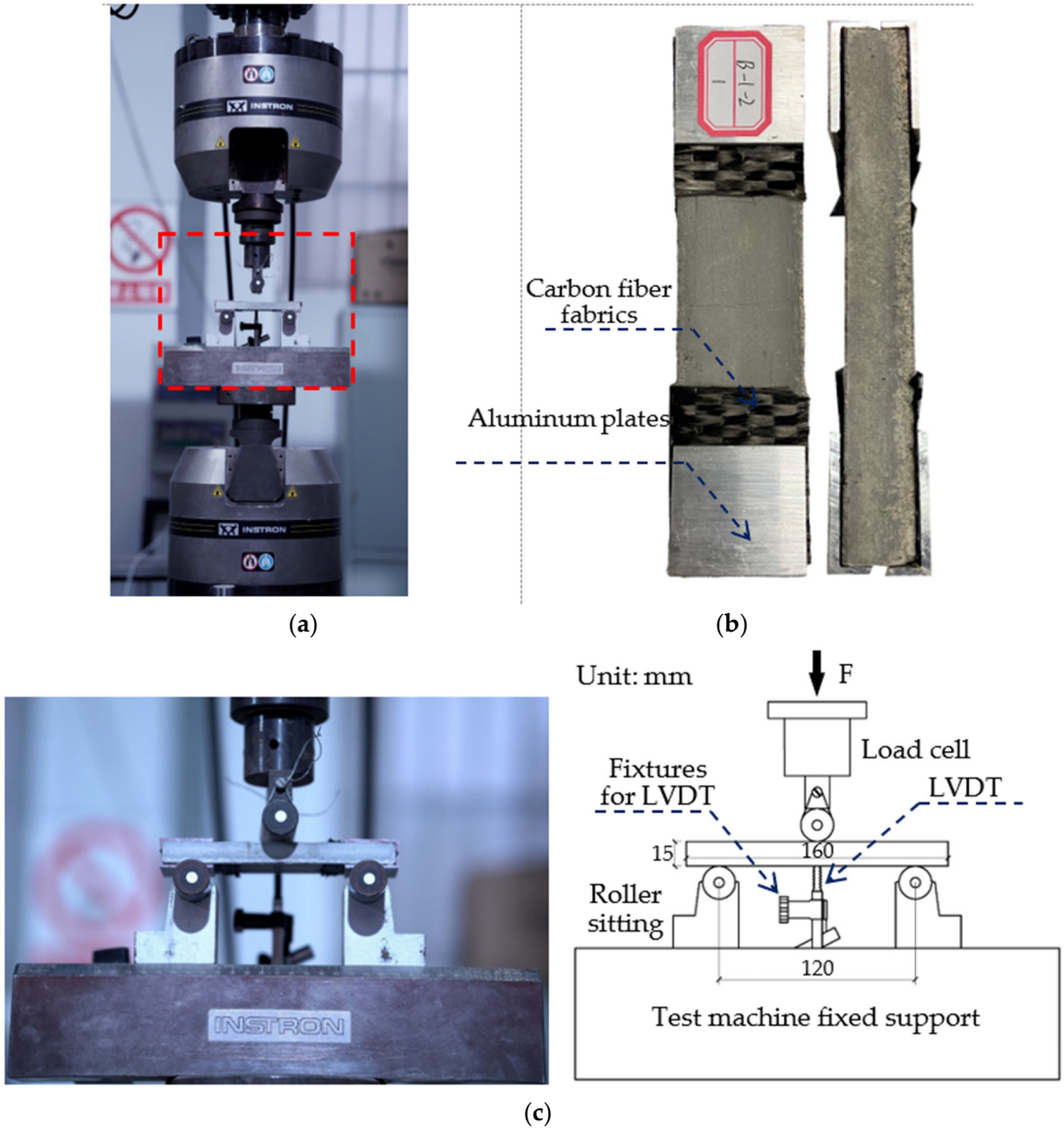


Figure 6. Loading configuration: (**a**) INSTRON-8802 Electro-hydraulic Servo Fatigue Testing Machine; (**b**) specimens; (**c**) detailed diagram of the content in the red box of (**a**).

4. Results

In accordance with the aforementioned treatment, three-point flexural tests were conducted on the specimens sequentially to investigate the impact of the fiber bundle number and the twist factor on the flexural properties of TLTP-FRCC. This study not only examined the macroscopic test phenomena and load–deflection curves for various working conditions but also calculated the equivalent bending stress and flexural failure toughness according to ASTM C1609/C1609M-19a [42] for a more quantitative comparison. Furthermore, to investigate the toughening mechanism of the through-length twisted PVA fibers during bending failure, MXCT observations were conducted on the bent specimens, and the corresponding analysis is presented in this paper.

4.1. Macroscopic Phenomena of Bending Damage

This type of cement-based specimen, which lacks coarse aggregate and has a low PVA fiber volume fraction, exhibited brittle rupture during the bending tests similar to plain concrete. Due to limited space, Figure 7 presents the bending damage of typical specimens in 12 working conditions. As the load on the top surface of the specimen increased, so

did the tensile stress on the cross-section below the neutral axis. Eventually, small cracks began to appear on the bottom surface, indicating that the specimen was losing its bending capacity, as shown in the left figure of Figure 7. Subsequently, as the loading displacement further increased, the specimen experienced rupture, as depicted in the middle figure of Figure 7. Moreover, the cross-sectional view resulting from the rupture is presented in the right figure of Figure 7. The cross-sections of the specimens were highly irregular due to the presence of the through-length PVA fibers, despite the brittle nature of the rupture.

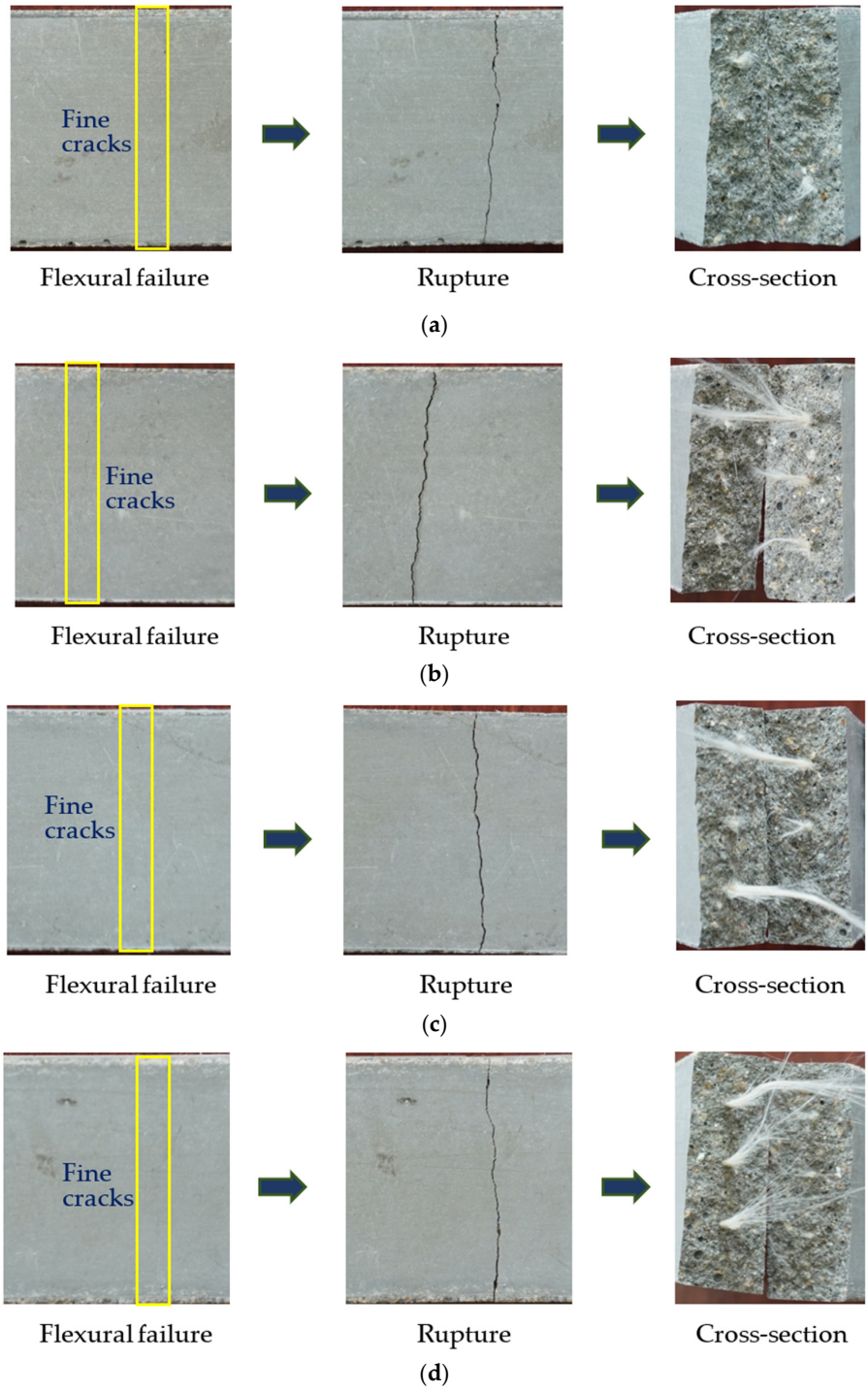


Figure 7. Morphology from flexural failure to rupture and the resulting cross-section of: (**a**) B-3-1-1; (**b**) B-3-2-3; (**c**) B-3-3-3; (**d**) B-3-4-2.

When examining the cross-sections of the specimens without twisting, as shown in Figure 7a, it is apparent that a majority of the fiber filaments within the fiber bundles were broken at this location, leading to flat fiber bundle sections. However, when the fiber bundles were twisted, the rupture caused the fiber bundle to deconvolute, resulting in an uneven section with fiber filaments of different lengths. This phenomenon is clearly visible in the bending rupture of B-3-4-2, as shown in Figure 8. As the twist factor increased, there was an increase in the number of filaments with different fiber positions within the same section of a single fiber bundle, as well as an increase in the variation among different fiber positions. This can lead to unevenness in the broken section of the fiber bundle, and longer, more fragmented broken filaments, as depicted in Figure 7b–d. For specimens containing more than one fiber bundle, the fiber damage pattern was different due to variations in the twist pattern and concrete fracture surface. For instance, in Figure 7a, B-3-1-1 exhibited an inclined fracture surface, indicating the presence of not only tensile stress but also shear stress. As a result, the lower fiber bundle was not fractured as cleanly as the upper bundle, and some fibers broke at the non-fracture surface. Therefore, the long-broken filaments on the fracture surface are primarily attributable to two factors: the displacement of different filaments within the fiber bundle due to fiber twisting, and the fracture of filaments on the non-fracture surface, often resulting from significant shear stresses. The filament breakage of different fiber bundles within the same specimen is not consistently on one side. As shown in Figure 7b,d, the filament breakage occurred on one side of the specimen cross-section, while in Figure 7c, the filament breakage appeared on both sides. Notably, in Figure 7c, the three fiber bundles exhibited three distinct cases of filament breakage. Specifically, the upper-side fiber bundle experienced partial breakage on the left side of the specimen, the middle-side fiber bundle broke almost completely at the fracture surface, and the lower-side fiber bundle experienced partial breakage on the right side of the specimen.



Figure 8. Deconvolution of fiber bundles in B-3-4-2 due to bending.

4.2. Flexural Toughness and Load–Deflection Curve

To enable a quantitative comparison among the specimens with different fiber bundle numbers and twist factors in the bending test, two evaluation indices for flexural toughness, equivalent bending stress, and energy consumption capacity were introduced. The effects of the fiber bundle number and twist factor on deflection tolerance, load capacity, equivalent bending stress, and energy consumption capacity were compared by holding the twist factor and fiber bundle number constant for each comparison.

4.2.1. Toughness Evaluation

Due to the low fiber volume fraction of fiber-reinforced concrete, its damage mode is similar to that of plain concrete, exhibiting no obvious plastic segment and brittle failure. Based on the load–deflection curves presented in Section 4.2.2, the critical points for analysis were chosen according to ASTM C1609/C1609M-19a [42], which included $L/1000$ (0.12 mm), $L/600$ (0.20 mm), and the peak point of each curve. Among these, the point of the maximum load is referred to as the limit of proportionality (LOP) [43]. The load values at $L/1000$ and $L/600$, as well as at the LOP, are denoted as $F_{L/1000}$, $F_{L/600}$, and F_{LOP}, respectively, while the corresponding deflection values are denoted as $\delta_{L/1000}$, $\delta_{L/600}$, and δ_{LOP}. According to ASTM C1609/C1609M-19a, the equivalent bending stress at the LOP was calculated using Equation (1) and denoted as f_{LOP}. Additionally, the energy consumption up to a certain point on the load–deflection curve is defined as the area under the curve up to that point. When the point is the LOP, the energy consumption is denoted as E_{LOP}, and can be calculated using Equation (2). This definition is consistent with the ASTM standard definition for toughness at various points on the load–deflection curve [42].

$$f_{LOP} = F_{LOP} \cdot \frac{L}{bh^2}, \tag{1}$$

$$E_{LOP} = \int_0^{\delta_{LOP}} F d\delta, \tag{2}$$

where L represents the clear span length, b denotes the width of the specimen, h represents the height of the specimen, and (δ, F) denotes a point on the load–deflection curve.

4.2.2. Bundle Number

The average load–deflection curves of 1 to 3 fiber bundles at twist factors of 0, 50, 100, and 150 are presented in Figure 9. The vertical axis represents both the load value and the equivalent bending stress, which was calculated using Equation (1) and is displayed on the right vertical axis. To enhance visibility, Figure 9 includes two vertical reference lines corresponding to $L/1000$ and $L/600$. The specimens could generally withstand deflections ranging from 0.21 to 0.34 mm and loads ranging from 0.38 to 0.77 kN. Due to the low volume fraction of PVA fibers and the absence of coarse aggregates in the TLTP-FRCC-based specimens, bending failure occurred in a manner similar to that of the plain concrete specimens, resulting in load–deflection curves that lack an obvious toughness segment. Instantaneous bending failure to specimen rupture means that only the state change prior to bending failure requires consideration in this paper. To simplify the notation, the twist factors of 0, 50, 100, and 150 are abbreviated as T1, T2, T3, and T4, respectively, while the fiber bundle numbers of 1, 2, and 3 are abbreviated as B1, B2, and B3. The average deflection δ, load F, equivalent bending stress f, and energy consumption E of the specimens at the three characteristic points ($L/1000$, $L/600$, and LOP) for the 12 working conditions are presented in Tables 4–6 for a better quantitative comparison.

At the $L/1000$ point, the average load force (equivalent bending stress) of the T1 specimens remained almost constant, ranging from 0.15 kN (2.04 MPa) to 0.15 kN (1.99 MPa) as the number of fiber bundles increased, before finally increasing to 0.16 kN (2.20 MPa). The average load force (equivalent bending stress) of the T2, T3, and T4 specimens sequentially increased with the increase in fiber bundles, ranging from 0.20 kN (2.65 MPa) to 0.26 kN (3.47 MPa), 0.15 kN (2.04 MPa) to 0.23 kN (3.07 MPa), and 0.31 kN (4.08 MPa) to 0.32 kN (4.25 MPa), respectively. Additionally, at the $L/1000$ point, the average energy consumption of the T1, T2, T3, and T4 specimens increased with the increase in fiber bundles, with specific energy consumption values shown in Tables 4–6.

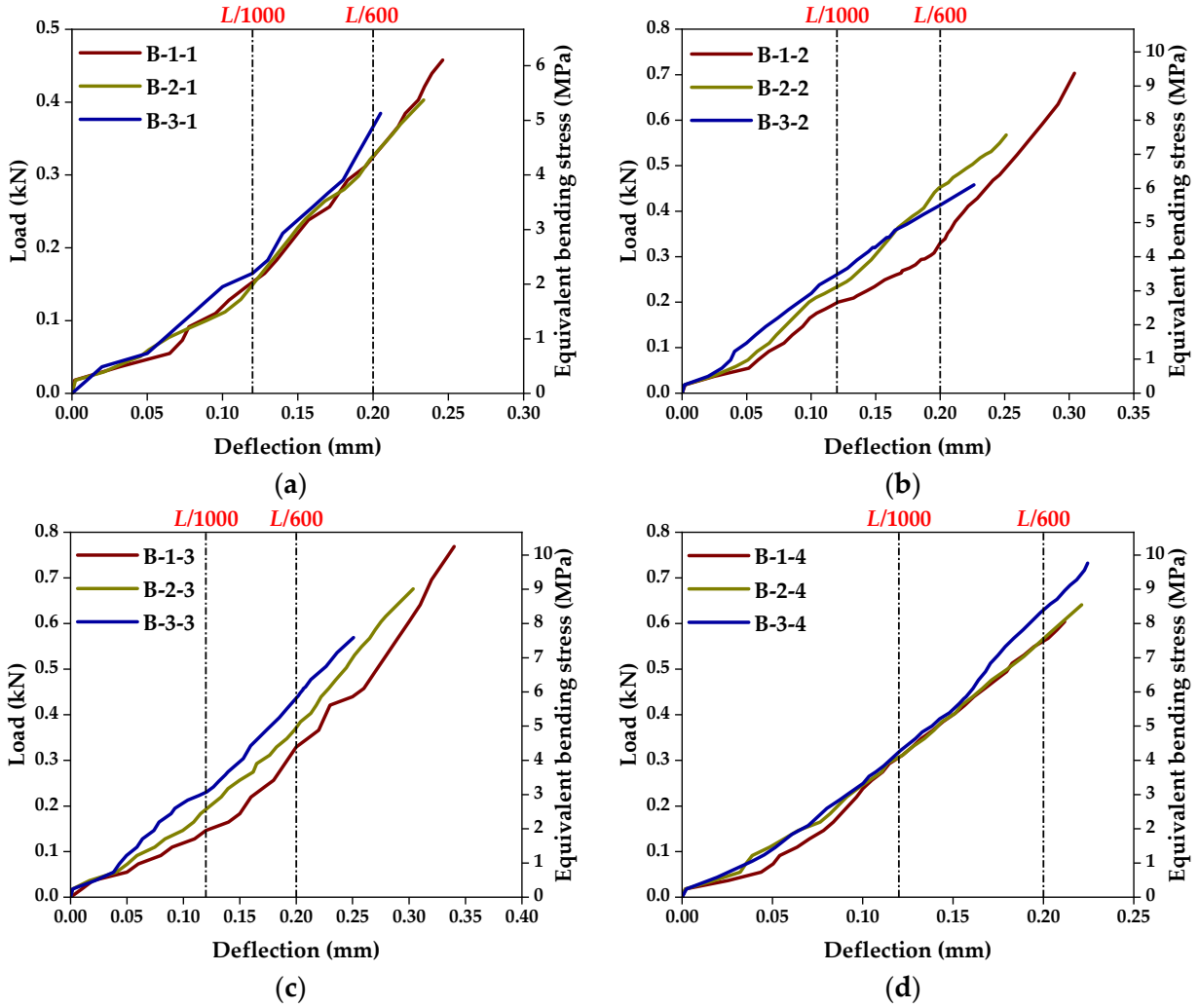


Figure 9. Average load–deflection curves with different fiber bundles when twist factor was: (**a**) 0; (**b**) 50; (**c**) 100; (**d**) 150.

Table 4. Average response quantities for flexural behavior of specimens (bundle number = 1).

Deflection	Indicator	B-1-1	B-1-2	B-1-3	B-1-4
$L/1000$	$\delta_{L/1000}$ (mm)	0.12	0.12	0.12	0.12
	$F_{L/1000}$ (kN)	0.15	0.20	0.15	0.31
	$f_{L/1000}$ (MPa) [a]	2.04	2.65	2.04	4.08
	$E_{L/1000}$ (J) [b]	0.0083	0.0108	0.0088	0.0147
$L/600$	$\delta_{L/600}$ (mm)	0.20	0.20	0.20	0.20
	$F_{L/600}$ (kN)	0.32	0.33	0.33	0.56
	$f_{L/600}$ (MPa)	4.33	4.40	4.39	7.49
	$E_{L/600}$ (J)	0.0274	0.0310	0.0263	0.0494
LOP	δ_{LOP} (mm)	0.25	0.30	0.34	0.21
	F_{LOP} (kN)	0.46	0.70	0.77	0.60
	f_{LOP} (MPa)	6.10	9.37	10.25	8.06
	E_{LOP} (J)	0.0453	0.0835	0.0991	0.0563

[a]: The value of "f" at each point was calculated based on the relevant "F" before rounding. [b]: The value of "E" at each point was calculated using the corresponding unrounded load and deflection values via MATLAB R2020b.

Table 5. Average response quantities for flexural behavior of specimens (bundle number = 2).

Deflection	Indicator	B-2-1	B-2-2	B-2-3	B-2-4
$L/1000$	$\delta_{L/1000}$ (mm)	0.12	0.12	0.12	0.12
	$F_{L/1000}$ (kN)	0.15	0.23	0.19	0.31
	$f_{L/1000}$ (MPa) [a]	1.99	3.12	2.57	4.09
	$E_{L/1000}$ (J) [b]	0.0086	0.0131	0.0111	0.0169
$L/600$	$\delta_{L/600}$ (mm)	0.20	0.20	0.20	0.20
	$F_{L/600}$ (kN)	0.33	0.45	0.37	0.57
	$f_{L/600}$ (MPa)	4.34	6.03	4.95	7.55
	$E_{L/600}$ (J)	0.0279	0.0401	0.0334	0.0518
LOP	δ_{LOP} (mm)	0.23	0.25	0.30	0.22
	F_{LOP} (kN)	0.40	0.57	0.68	0.64
	f_{LOP} (MPa)	5.37	7.57	9.01	8.55
	E_{LOP} (J)	0.0402	0.0659	0.0882	0.0646

[a]: The value of "f" at each point was calculated based on the relevant "F" before rounding. [b]: The value of "E" at each point was calculated using the corresponding unrounded load and deflection values via MATLAB R2020b.

Table 6. Average response quantities for flexural behavior of specimens (bundle number = 3).

Deflection	Indicator	B-3-1	B-3-2	B-3-3	B-3-4
$L/1000$	$\delta_{L/1000}$ (mm)	0.12	0.12	0.12	0.12
	$F_{L/1000}$ (kN)	0.16	0.26	0.23	0.32
	$f_{L/1000}$ (MPa) [a]	2.20	3.47	3.07	4.25
	$E_{L/1000}$ (J) [b]	0.0099	0.0158	0.0142	0.0173
$L/600$	$\delta_{L/600}$ (mm)	0.20	0.20	0.20	0.20
	$F_{L/600}$ (kN)	0.37	0.41	0.44	0.63
	$f_{L/600}$ (MPa)	4.88	5.51	5.82	8.39
	$E_{L/600}$ (J)	0.0305	0.0431	0.0405	0.0546
LOP	δ_{LOP} (mm)	0.21	0.23	0.25	0.22
	F_{LOP} (kN)	0.38	0.46	0.57	0.73
	f_{LOP} (MPa)	5.13	6.10	7.59	9.77
	E_{LOP} (J)	0.0324	0.0545	0.0662	0.0711

[a]: The value of "f" at each point was calculated based on the relevant "F" before rounding. [b]: The value of "E" at each point was calculated using the corresponding unrounded load and deflection values via MATLAB R2020b.

At the $L/600$ point, the T1 specimens showed a sequential increase in the average load force (equivalent bending stress), ranging from 0.32 kN (4.33 MPa) to 0.33 kN (4.34 MPa) and 0.37 kN (4.88 MPa) with increasing fiber bundles. The average load force (equivalent bending stress) of T2 specimens increased from 0.33 kN (4.40 MPa) to 0.45 kN (6.03 MPa) with increasing fiber bundles before decreasing to 0.41 kN (5.51 MPa). For T3 and T4, the average load force (equivalent bending stress) of the specimens also increased sequentially with increasing fiber bundles, ranging from 0.33 kN (4.39 MPa) to 0.44 kN (5.82 MPa), 0.56 kN (7.49 MPa) to 0.63 kN (8.39 MPa), respectively. Similarly, the average energy consumption of T1, T2, T3, and T4 increased with the increase in the number of fiber bundles at the $L/600$ point, and the specific energy consumption values are shown in Tables 4–6.

Regarding the LOP, deflection tolerance is a crucial evaluation index. As the fiber bundles increased, the T1, T2, and T3 deflection tolerance values at the LOP point decreased, while that of T4 remained constant. The average load force (equivalent bending stress) of the T1 specimens decreased from 0.46 kN (6.10 MPa) to 0.38 kN (5.13 MPa), and T2 and T3 decreased from 0.70 kN (9.37 MPa) and 0.77 kN (10.25 MPa) to 0.46 kN (6.10 MPa) and 0.57 kN (7.59 MPa), respectively. Conversely, the average load force (equivalent bending stress) of T4 increased from 0.60 kN (8.06 MPa) to 0.73 kN (9.77 MPa) as the fiber bundles increased. For the LOP point, the average energy consumption of T1, T2, and T3 decreased with the increase in the fiber bundles, while for T4, the energy consumption capacity increased, as shown in Tables 4–6.

4.2.3. Twist Factor

In the preceding section, the twist factor was kept constant to compare the effects of different fiber bundle numbers. In this section, the number of fiber bundles remained constant to evaluate the effects caused by varying twist factors. To improve clarity, vertical reference lines at $L/1000$ and $L/600$ are plotted in Figure 10, which presents the average load–deflection curves for fiber bundles ranging from 1 to 3 with twist factors of 0, 50, 100, and 150.

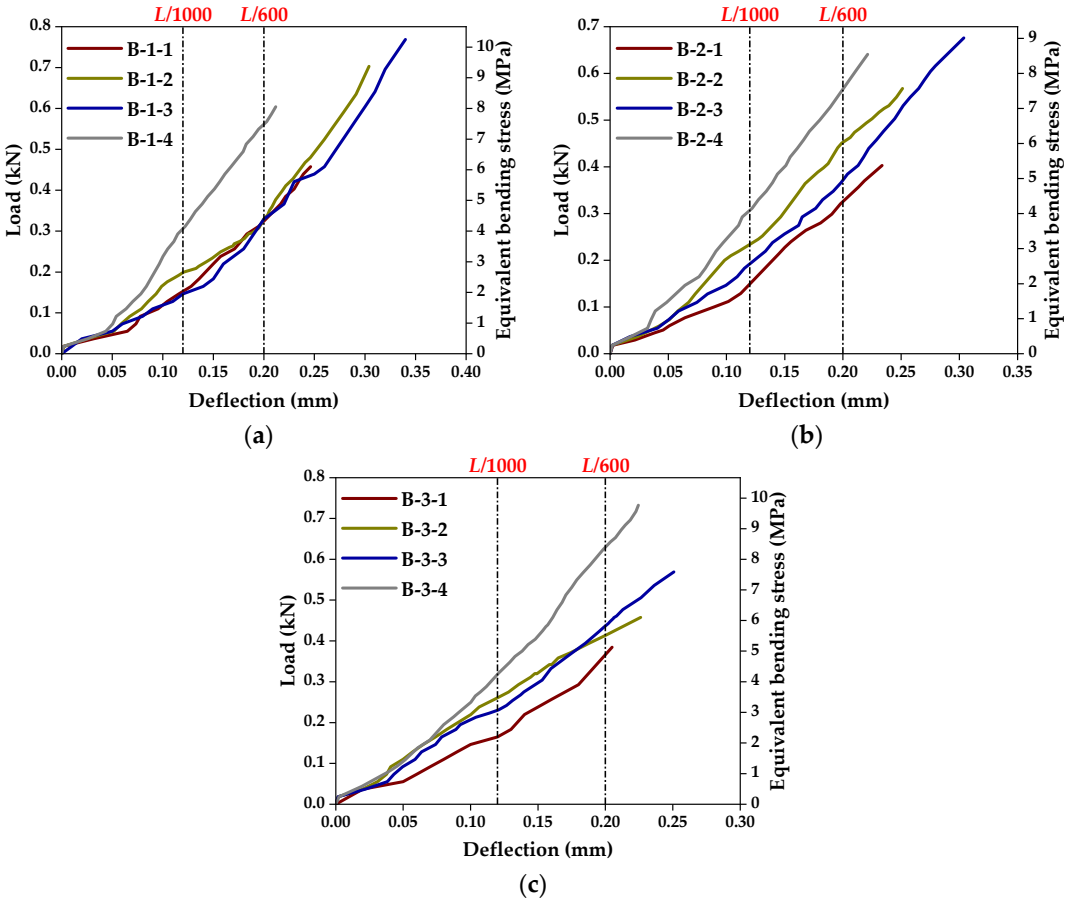


Figure 10. Average load–deflection curves with different twist factors when bundle number is: (**a**) 1; (**b**) 2; (**c**) 3.

At the $L/1000$ point, the average load force, equivalent bending stress, and energy consumption of B1, B2, and B3 initially increased, followed by a decrease, and then another increase with the increasing twist factor. At the $L/600$ point, the same trend was observed for B1, B2, and B3, except for the average load force and equivalent bending stress of B3, which increased continually with the increasing twist factor. At the LOP point, the average load force, equivalent bending stress, and energy consumption of B1 and B2 increased as the twist factor increased from 0 to 100, but then decreased as the twist factor increased further. In contrast, for B3, these values continuously increased with the increasing twist factor. The specific values for each index are provided in Tables 4–6.

4.3. Microscopic Phenomena of Bending Damage

In addition to analyzing the macroscopic tests, this section presents the results of observing the specimens that failed in bending using MXCT as described in Section 2.3. Due to spatial limitations, this paper presents the MXCT results for the most representative B-3-4-2 specimen, as illustrated in Figure 11. The top and bottom surfaces of the 3D specimen, obtained through 3D reconstruction of the original MXCT figures, are depicted

in Figure 11a,b. By comparing Figure 11b with the middle figure in Figure 7d, it can be observed that the 3D reconstruction accurately reproduced the cracks on the bottom surface of the specimen. In Figure 11c, it can be observed that the specimen remained intact and the fibers were still under tension even after the specimen failed in bending. To better observe the damage of the PVA fibers, three fibers from the top to bottom were analyzed by increasing the display magnification one by one, and the resulting damage morphology diagrams are shown in Figure 11d–f. Upon examination of the aforementioned figures, it is apparent that the location of the fiber damage is situated at the cracks in the cementitious composites. This was due to the tensile stress at this location exceeding the allowable tensile stress value of the TLTP-FRCC-based specimen. Additionally, along with the cracking of the concrete, the fiber filaments in the fiber bundle were also pulled off. The fiber damage segment in the yellow box reveals that the fiber damage at the crack was the most significant, and the residual fiber filaments were the least. The fiber filaments gradually increased towards the two longitudinal extensions of the fiber bundle and show a spatially uneven increase mode. The damage to the three fibers shows a gradual increase from bottom to top, which corresponds to the higher shear stress in the upper part of the specimen shown in Figure 11b, which led to the tilting of the crack.

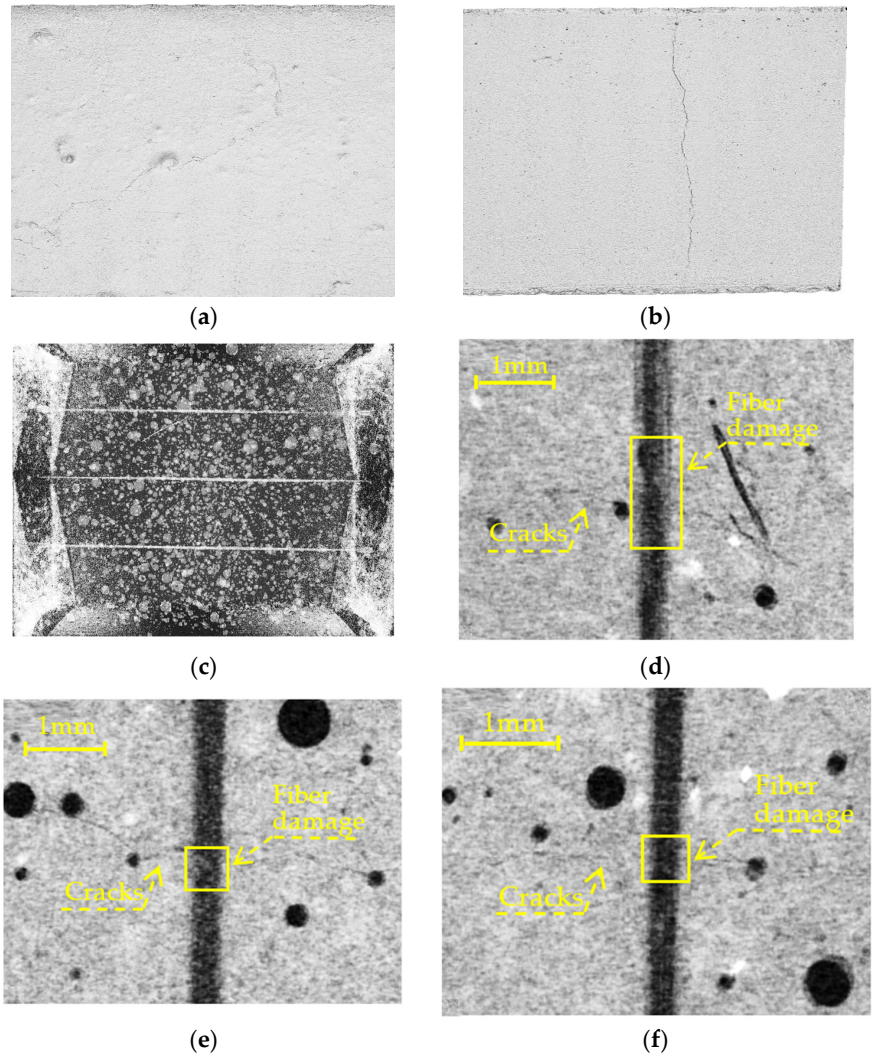


Figure 11. MXCT results of B-3-4-2 at the point of bending failure: (**a**) top surface; (**b**) bottom surface; (**c**) interior of the specimen from perspective view; (**d**) damage details of the top fiber in (**c**); (**e**) damage details of the middle fiber in (**c**); (**f**) damage details of the bottom fiber in (**c**).

5. Discussion

Upon conducting the bending test, it became apparent that this TLTP-FRCC, which lacks coarse aggregates and has a low fiber volume fraction, developed only a single prominent fine crack on the specimen surface at the moment of bending failure. As loading displacement increased, the specimen subsequently fractured directly. Nevertheless, based on the unevenness of the cross-section resulting from the rupture, it can be inferred that the through-length twisted fibers contributed to toughening the composite during the bending test, as the concrete experienced both tensile and shear stresses.

When the same twist factor was applied to the fibers, and more fiber bundles were introduced, the vertical load and energy consumption increased at relatively small deflections of the specimen (such as the control points at $L/1000$ and $L/600$), owing to the increased stiffness of the FRCC and its consequent increased modulus of elasticity [44]. However, as the deflection continued to increase and the LOP point of the specimen was reached, the thick fiber bundles (up to 0.8 mm in cross-sectional width without twisting) played a similar role as the initial defect and led to a decrease in the elastic modulus of the specimen, because the relatively smooth fiber bundles did not have a strong enough bond with the cementitious matrix [45]. As the fiber twist factor increased, the fiber bundle slowly transformed into a spiral, resulting in a decrease in the radius and an increase in the contacted fiber with the cementitious matrix. Simultaneously, the roughness of the contact surface increased. These factors operated in tandem to enhance the bond between the fiber and the matrix, effectively mitigating the slippage effect. After applying the toughening mechanism discussed above, the bending test produced the following results. When the deflection was relatively small, the bonding performance between the fiber and the matrix was not a critical factor, and the specimens with four different twist factors generally exhibited an increasing trend in toughness and modulus of elasticity as the fiber bundle increased. As the deflection value gradually approached the bending tolerance, the requirement for bonding performance significantly increased, and specimens with twist factors of 0, 50, and 100 tended to exhibit decreased toughness and elastic modulus as the fiber bundle increased due to inadequate bonding performance and the fiber resembling the initial defect. However, when the twist factor was increased to 150, this trend was accompanied by an increase in the fiber and matrix bond strength, resulting in a favorable trend of increasing toughness and elastic modulus as the fiber bundle increased. With regard to the deflection values of bending failure, the test results are consistent with the above description, where the value decreased with an increasing number of fiber bundles at low twist factors (0, 50, 100), and at high twist factor equal to 150, the twisting could largely counteract the effect of the defects caused by the fiber bundles. It is worth noting that when the $L/600$ point is very close to the LOP point of a specimen, the effect of the fiber defects caused by insufficient twists will start to affect the $L/600$ state of the specimen. For example, the average load (equivalent bending stress) of B-3-2 was smaller than that of B-2-2 at the $L/600$ point. The LOP point is a key point used to measure the flexural toughness of the specimen, and the absolute values of deflection, equivalent bending stress, and bending energy consumption at the LOP point for the specimens under different working conditions are given in Figure 12, along with their relative proportions compared to the average values of B-1-1.

To put it in another perspective, the effects of different twist factors with the same number of fiber bundles are discussed further. As mentioned previously, twisted fibers increased the toughness and elastic modulus of the TLTP-FRCC specimens based on the larger contact area and rougher contact surface between the fiber and the matrix. However, since the thickness of a flexural beam is much smaller than its width, a twisted fiber bundle with a large height will instead lead to a significant loss of toughness and elastic modulus. Hence, at the LOP point, specimens with the same number of fiber bundles exhibited an augmentation in the bending capacity and energy consumption capacity as the fiber twist factor increased from 0 to 100. This increase can be attributed to the gradual reduction of the slippage effect. However, when the twist factor reached 150, there was a sharp

decrease in the bending and energy consumption capacity of the B1 specimens due to their excessive fiber bundle height. Fortunately, this issue can be solved by increasing the fiber bundles, as cross rows of multiple fibers can enhance the cross-sectional stiffness despite the fiber bundle defects and also consume more energy through filament pulled-off, as shown in Figure 11. Therefore, as the twist factor reached 150, the decrease in the bending and energy consumption capacity of the B2 specimens slowed down significantly, and the corresponding capacity of the B3 specimens increased even more.

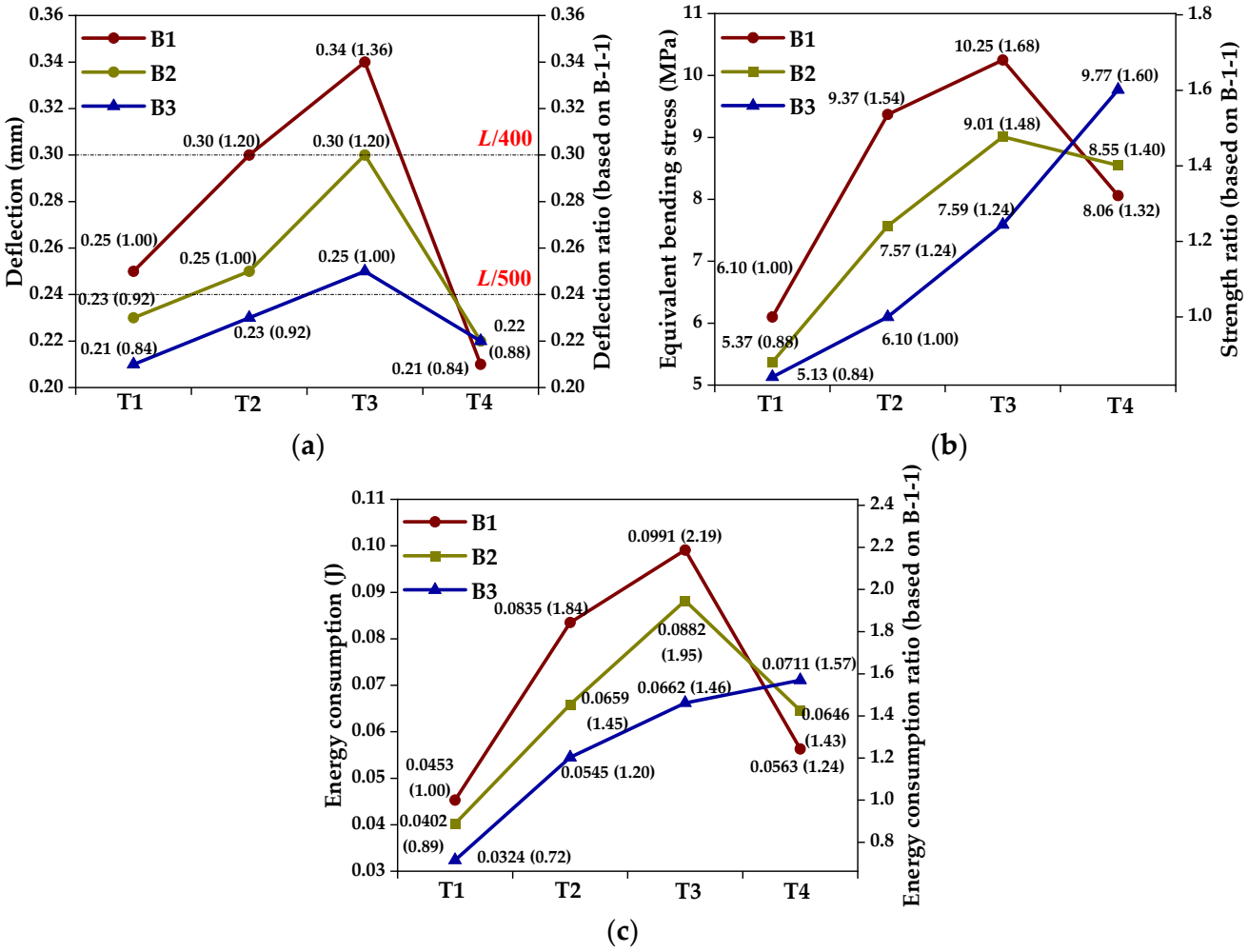


Figure 12. Absolute and relative values (based on the average values of B-1-1) at the LOP point for specimens under different working conditions of: (**a**) deflection; (**b**) equivalent bending stress; (**c**) energy consumption.

For the cementitious composites used, PVA fiber bundles with 1000 filaments per bundle, oriented along the length of the specimens, had a significant impact on the results due to defects in the transverse and vertical directions caused by their placement in the matrix or by excessive twisting. By considering these negative effects along with the toughening effect of the TLTP fiber bundles, this paper concludes that the best flexural behaviors were obtained for the B-1-3 specimens, considering various factors in general. In the upcoming research, the impact of different filament quantities within a PVA fiber bundle on flexural performance will be examined. These investigations will be tailored to the height of the specimens to accurately determine their influence. Moreover, beam, column, wall, and joint members made of TLTP-FRCC with the best-performing match will be designed to further verify their performance at the structural member level.

6. Conclusions

TLTP-FRCC exhibits promising potential for use in ductile precast concrete components and other applications, owing to its significantly enhanced flexural mechanical properties and bending toughness. Based on the results of the three-point bending tests, specimens with a twist factor of 100 and a single fiber bundle exhibited significantly improved flexural behavior, indicating a favorable pairing. MXCT observation revealed the microscopic toughening mechanisms of the twisted PVA fibers. In summary, this study concludes that:

(1) During the initial stage of the bending test, where the deflection was relatively small, the flexural properties and energy consumption capacities of the specimen increased with an increase in the fiber bundles. However, as the vertical deflection became larger, fiber bundles with an insufficient twist factor had a greater negative impact due to insufficient bonding with the matrix, leading to poorer flexural behavior of the specimen. Conversely, specimens with sufficient twisting can overcome this effect and fully utilize the reinforcing effect of the fiber bundles.

(2) By increasing the contact area and roughness of the contact surface between the PVA fibers and the cementitious composite matrix, twisting the fibers can improve the flexural properties and bending toughness of FRCC. However, excessively high twist factors can lead to relatively thick fiber bundles, which can be more sensitive to defects in the height direction of specimens with small height-to-width ratios, resulting in a deterioration of flexural behavior. This problem can be addressed through the overall cross-sectional effect of multiple fiber bundles.

(3) To better compare the effect of the fiber twist factor on the interaction mechanism of specimens, this study only considered conditions with a low number of fiber bundles, resulting in a lower fiber volume dosage. Nevertheless, the flexural performance and energy consumption capacity of the specimens were significantly enhanced with the appropriate matching of the twist factor and bundle number. This enhancement included a 36% increase in deflection, 68% higher equivalent bending stress, and a 119% rise in energy consumption compared to the untwisted PVA fiber specimens.

This study focused on long fiber bundle-reinforced concrete. The fiber bundle in this experiment gave full use of its tensile strength. The effect of different twisted fiber bundles for the production and design of ductile precast concrete components can be a reference, and these ductile components in engineering and maintenance structures can significantly enhance the safety and protection performance.

Author Contributions: Conceptualization, methodology, resources, supervision, project administration, funding acquisition, writing—review and editing, H.Z.; conceptualization, methodology, software, formal analysis, investigation, data curation, visualization, writing—original draft preparation, F.H.; supervision, funding acquisition, writing—review and editing, Y.D.; investigation, resources, visualization, J.Y.; investigation, Z.D.; investigation, L.C. All authors have read and agreed to the published version of the manuscript.

Funding: This research was funded by the National Key R&D Program of China (Grant No. 2019YFE0112600), the National Natural Science Foundation of China (Grant No. 52078459), and the National Natural Science Foundation of Zhejiang Province (Grant Nos. LZ22E080005, LHZ23E080003).

Data Availability Statement: The data presented in this study are available upon request from the corresponding author.

Acknowledgments: The authors acknowledge the efforts of the reviewers to improve the quality of this paper.

Conflicts of Interest: The authors declare no conflict of interest.

Abbreviations

PVA, polyvinyl alcohol; FRCC, fiber-reinforced cementitious composite; TLTP, through-length twisted PVA; ESEM, environmental scanning electron microscopy; MXCT, micro-X-ray computed tomography; LVDT, linear variable displacement transducer; LOP, limit of proportionality; T1, twist factor of 0; T2, twist factor of 50; T3, twist factor of 100; T4, twist factor of 150; B1, fiber bundle number of 1; B2, fiber bundle number of 2; B3, fiber bundle number of 3.

References

1. Sonat, C.; Kumar, D.; Koh, W.C.; Li, J.X.; Unluer, C.; Yang, E.H. Strain hardening magnesium-silicate-hydrate composites with extremely low fiber dosage of 0.5% by volume. *Cem. Concr. Compos.* **2023**, *142*, 105200. [CrossRef]
2. Zhang, P.; Han, X.; Zheng, Y.X.; Wan, J.Y.; Hui, D. Effect of PVA fiber on mechanical properties of fly ash-based geopolymer concrete. *Rev. Adv. Mater. Sci.* **2021**, *60*, 418–437. [CrossRef]
3. Li, L.; Wei, Y.J.; Feng, Q.; Liu, F.; Liu, B.; Pu, B.C. A review: Progress in molecular dynamics simulation of portland cement (geopolymer)-based composites and the interface between these matrices and reinforced material. *Buildings* **2023**, *13*, 1875. [CrossRef]
4. Zhou, A.; Yu, Z.C.; Wei, H.N.; Tam, L.H.; Liu, T.J.; Zou, D.J. Understanding the toughening mechanism of silane coupling agents in the interfacial bonding in steel fiber-reinforced cementitious composites. *ACS Appl. Mater. Interfaces* **2020**, *12*, 44163–44171. [CrossRef]
5. Zhang, H.M.; Hu, F.; Duan, Y.F.; Shi, D.W.; Hu, G.M. Metaheuristic optimization algorithm for rapid parameter identification of the Bouc-Wen model for self-centering shear walls. *Int. J. Struct. Stab. Dyn.* **2022**, *22*, 2350041. [CrossRef]
6. Zeybek, O.; Ozkilic, Y.O.; Celik, A.I.; Deifalla, A.F.; Ahmad, M.; Sabri, M.M.S. Performance evaluation of fiber-reinforced concrete produced with steel fibers extracted from waste tire. *Front. Mater.* **2022**, *9*, 1057128. [CrossRef]
7. Ozkilic, Y.O.; Beskopylny, A.N.; Stel'makh, S.A.; Shcherban', E.M.; Mailyan, L.R.; Meskhi, B.; Chernil'nik, A.; Ananova, O.; Aksoylu, C.; Madenci, E. Lightweight expanded-clay fiber concrete with improved characteristics reinforced with short natural fibers. *Case Stud. Constr. Mater.* **2023**, *19*, e02367.
8. Shcherban', E.M.; Stel'makh, S.A.; Beskopylny, A.N.; Mailyan, L.R.; Meskhi, B.; Shilov, A.A.; Chernil'nik, A.; Ozkilic, Y.O.; Aksoylu, C. Normal-weight concrete with improved stress-strain characteristics reinforced with dispersed coconut fibers. *Appl. Sci.* **2022**, *12*, 11734. [CrossRef]
9. Tran, T.K.; Kim, D.J.; Choi, E. Behavior of double-edge-notched specimens made of high performance fiber reinforced cementitious composites subject to direct tensile loading with high strain rates. *Cem. Concr. Res.* **2014**, *63*, 54–66. [CrossRef]
10. Yao, X.L.; Pei, Z.Y.; Zheng, H.Y.; Guan, Q.Z.; Wang, F.P.; Wang, S.; Ji, Y.C. Review of mechanical and temperature properties of fiber reinforced recycled aggregate concrete. *Buildings* **2022**, *12*, 1224. [CrossRef]
11. Zhang, K.; Ni, T.; Zhang, J.; Wang, W.; Chen, X.; Zaccariotto, M.; Yin, W.; Zhu, S.X.; Galvanetto, U. Experimental and hybrid FEM/peridynamic study on the fracture of ultra-high-performance concretes reinforced by different volume fractions of polyvinyl alcohol fibers. *Polymers* **2023**, *15*, 501. [CrossRef] [PubMed]
12. Prakash, R.; Thenmozhi, R.; Raman, S.N.; Subramanian, C. Characterization of eco-friendly steel fiber-reinforced concrete containing waste coconut shell as coarse aggregates and fly ash as partial cement replacement. *Struct. Concr.* **2020**, *21*, 437–447. [CrossRef]
13. Sekar, K.C.; Murugesan, R.; Sivaraja, M.; Prakash, R. Development of sustainable concrete from hypo sludge combined with basalt fibre and latex. *Sustainability* **2023**, *15*, 10986. [CrossRef]
14. Tran, T.K.; Kim, D.J. High strain rate effects on direct tensile behavior of high performance fiber reinforced cementitious composites. *Cem. Concr. Compos.* **2014**, *45*, 186–200. [CrossRef]
15. Shao, Y.; Billington, S.L. Predicting the two predominant flexural failure paths of longitudinally reinforced high-performance fiber-reinforced cementitious composite structural members. *Eng. Struct.* **2019**, *199*, 109581. [CrossRef]
16. Yoo, D.Y.; Banthia, N. Mechanical properties of ultra-high-performance fiber-reinforced concrete: A review. *Cem. Concr. Compos.* **2016**, *73*, 267–280. [CrossRef]
17. Prakash, R.; Divyah, N.; Srividhya, S.; Avudaiappan, S.; Amran, M.; Raman, S.N.; Guindos, P.; Vatin, N.I.; Fediuk, R. Effect of steel fiber on the strength and flexural characteristics of coconut shell concrete partially blended with fly ash. *Materials* **2022**, *15*, 4272. [CrossRef]
18. Divyah, N.; Thenmozhi, R.; Neelamegam, M.; Prakash, R. Characterization and behavior of basalt fiber-reinforced lightweight concrete. *Struct. Concr.* **2021**, *22*, 422–430. [CrossRef]
19. Shao, Y.; Nguyen, W.; Bandelt, M.J.; Ostertag, C.P.; Billington, S.L. Seismic performance of high-performance fiber-reinforced cement-based composite structural members: A review. *J. Struct. Eng.* **2022**, *148*, 03122004. [CrossRef]
20. Hou, L.J.; Xu, R.; Chen, D.; Xu, S.L.; Aslani, F. Seismic behavior of reinforced engineered cementitious composite members and reinforced concrete/engineered cementitious composite members: A review. *Struct. Concr.* **2020**, *21*, 199–219. [CrossRef]
21. Noushini, A.; Samali, B.; Vessalas, K. Effect of polyvinyl alcohol (PVA) fibre on dynamic and material properties of fibre reinforced concrete. *Constr. Build. Mater.* **2013**, *49*, 374–383. [CrossRef]

22. Zhang, P.; Yang, Y.H.; Wang, J.; Jiao, M.J.; Ling, Y.F. Fracture models and effect of fibers on fracture properties of cementitious composites-a review. *Materials* **2020**, *13*, 5495. [CrossRef] [PubMed]
23. Wang, L.; Guo, F.X.; Yang, H.M.; Wang, Y.; Tang, S.W. Comparison of fly ash, PVA fiber, MgO and shrinkage-reducing admixture on the frost resistance of face slab concrete via pore structural and fractal analysis. *Fractals-Complex Geom. Patterns Scaling Nat. Soc.* **2021**, *29*, 2140002. [CrossRef]
24. Ding, C.; Guo, L.P.; Chen, B. An optimum polyvinyl alcohol fiber length for reinforced high ductility cementitious composites based on theoretical and experimental analyses. *Constr. Build. Mater.* **2020**, *259*, 119824. [CrossRef]
25. Qiu, J.S.; Lim, X.N.; Yang, E.H. Fatigue-induced deterioration of the interface between micro-polyvinyl alcohol (PVA) fiber and cement matrix. *Cem. Concr. Res.* **2016**, *90*, 127–136. [CrossRef]
26. Cao, M.; Xie, C.; Li, L.; Khan, M. Effect of different PVA and steel fiber length and content on mechanical properties of $CaCO_3$ whisker reinforced cementitious composites. *Mater. Constr.* **2019**, *69*, e200. [CrossRef]
27. Wang, D.; Che, J.L.; Liu, H.F.; Chin, S.C. Enhanced ductility and toughness of desert sand engineered cementitious composites. *Buildings* **2023**, *13*, 1538. [CrossRef]
28. Kim, J.; Lee, G.P.; Moon, D.Y. Evaluation of mechanical properties of steel-fibre-reinforced concrete exposed to high temperatures by double-punch test. *Constr. Build. Mater.* **2015**, *79*, 182–191. [CrossRef]
29. Naaman, A.E. Engineered steel fibers with optimal properties for reinforcement of cement composites. *J. Adv. Concr. Technol.* **2003**, *1*, 241–252. [CrossRef]
30. Karalar, M.; Ozkilic, Y.O.; Deifalla, A.F.; Aksoylu, C.; Arslan, M.H.; Ahmad, M.; Sabri, M.M.S. Improvement in bending performance of reinforced concrete beams produced with waste lathe scraps. *Sustainability* **2022**, *14*, 12660. [CrossRef]
31. Chen, J.H.; Pakdel, E.; Xie, W.J.; Sun, L.; Xu, M.Y.; Liu, Q.Z.; Wang, D. High-performance natural melanin/poly(vinyl alcohol-co-ethylene) nanofibers/PA6 fiber for twisted and coiled fiber-based actuator. *Adv. Fiber Mater.* **2020**, *2*, 64–73. [CrossRef]
32. Haines, C.S.; Lima, M.D.; Li, N.; Spinks, G.M.; Foroughi, J.; Madden, J.D.W.; Kim, S.H.; Fang, S.L.; de Andrade, M.J.; Goktepe, F.; et al. Artificial muscles from fishing line and sewing thread. *Science* **2014**, *343*, 868–872. [CrossRef]
33. Yuan, J.K.; Poulin, P. Fibers do the twist. *Science* **2014**, *343*, 845–846. [CrossRef] [PubMed]
34. Du, W.P.; Yang, C.Q.; Wang, C.; Pan, Y.; Zhang, H.L.; Yuan, W.W. Flexural behavior of polyvinyl alcohol fiber-reinforced ferrocement cementitious composite. *J. Mater. Civ. Eng.* **2021**, *33*, 04021040. [CrossRef]
35. Zhang, M.; Deng, M.K.; Yang, J.S.; Zhang, Y.X. Experimental study on the shear behavior of reinforced highly ductile fiber-reinforced concrete beams with stirrups. *Buildings* **2022**, *12*, 1264. [CrossRef]
36. Guo, L.; Berglin, L.; Mattila, H. Improvement of electro-mechanical properties of strain sensors made of elastic-conductive hybrid yarns. *Text. Res. J.* **2012**, *82*, 1937–1947. [CrossRef]
37. Pang, Z.M.; Lu, C.; Liu, J.X.; Yao, Y.M.; Wang, J.J. Experimental study of tensile properties of strain-hardening cementitious composites (SHCCs) reinforced with innovative twisted basalt fibers. *Structures* **2023**, *48*, 1977–1988. [CrossRef]
38. Cao, M.L.; Xie, C.P.; Guan, J.F. Fracture behavior of cement mortar reinforced by hybrid composite fiber consisting of $CaCO_3$ whiskers and PVA-steel hybrid fibers. *Compos. Pt. A Appl. Sci. Manuf.* **2019**, *120*, 172–187. [CrossRef]
39. Qsymah, A.; Sharma, R.; Yang, Z.; Margetts, L.; Mummery, P. Micro X-ray computed tomography image-based two-scale homogenisation of ultra high performance fibre reinforced concrete. *Constr. Build. Mater.* **2017**, *130*, 230–240. [CrossRef]
40. Ye, J.D.; Liu, G.H. Pullout response of ultra-high-performance concrete with twisted steel fibers. *Appl. Sci.* **2019**, *9*, 658. [CrossRef]
41. *ISO 679*; Cement–Test Methods–Determination of Strength. ISO: Geneva, Switzerland, 2009.
42. *ASTM C1609/C1609M-19a*; Standard Test Method for Flexural Performance of Fiber-Reinforced Concrete (Using Beam with Third-Point Loading). ASTM International: West Conshohocken, PA, USA, 2019.
43. Kim, D.J.; Naaman, A.E.; El-Tawil, S. Comparative flexural behavior of four fiber reinforced cementitious composites. *Cem. Concr. Compos.* **2008**, *30*, 917–928. [CrossRef]
44. Laverde, V.; Marin, A.; Benjumea, J.M.; Ortiz, M.R. Use of vegetable fibers as reinforcements in cement-matrix composite materials: A review. *Constr. Build. Mater.* **2022**, *340*, 127729. [CrossRef]
45. Zhang, P.; Wei, S.Y.; Wu, J.J.; Zhang, Y.; Zheng, Y.X. Investigation of mechanical properties of PVA fiber-reinforced cementitious composites under the coupling effect of wet-thermal and chloride salt environment. *Case Stud. Constr. Mater.* **2022**, *17*, e01325. [CrossRef]

Disclaimer/Publisher's Note: The statements, opinions and data contained in all publications are solely those of the individual author(s) and contributor(s) and not of MDPI and/or the editor(s). MDPI and/or the editor(s) disclaim responsibility for any injury to people or property resulting from any ideas, methods, instructions or products referred to in the content.